

Long-term and multi-wavelength evolution of a changing-look AGN Mrk 1018

Bing Lyu,^{1,2} Zhen Yan,² Wenfei Yu,² Qingwen Wu,^{1*}

¹Huazhong University of Science and Technology, School of Physics, 1037 Luoyu Road, Wuhan, 430074, China

²Shanghai Astronomical Observatory, CAS, Nandan Road 80, Shanghai, 200030, China

Accepted XXX. Received YYY; in original form ZZZ

ABSTRACT

The physical mechanism for triggering the changing-look phenomenon in active galactic nuclei (AGNs) is still unclear. We explore this issue based on the multi-wavelength spectral and flux variations for a changing-look AGN Mrk 1018 with long-term observations in the X-ray, optical/ultraviolet(UV), and radio bands. Both the optical and the X-ray emission experience rapid decay in changing-look phase during 2010–2015, where a re-flare appears in the optical/UV and X-ray bands. We find a time lag of ~ 20 days of optical/UV behind X-ray variations in type 1.9 phase. The 5 GHz radio flux decreases by $\sim 20\%$ in type 1.9 phase during 2016–2017. We find both X-ray photon index (Γ) and the optical-to-X-ray spectral index (α_{ox}) are anti-correlated with the Eddington scaled 2–10 keV X-ray luminosity (L_X/L_{Edd}) in the type 1.9 phase. However, the type 1 phase deviates from these two anti-correlations, which suggests that the change of broad emission lines might be regulated by the evolution of accretion disk (e.g., disappearing of the inner cold disk in the type 1.9 phase).

Key words: galaxies: nuclei – galaxies: Seyfert – individual: Mrk 1018

1 INTRODUCTION

Type 1 and type 2 active galactic nuclei (AGNs) are classified based on the widths of optical spectral emission lines. Type 1 AGNs show both broad lines ($> 1000 \text{ km s}^{-1}$) and narrow lines ($< 1000 \text{ km s}^{-1}$), while type 2 AGNs show only narrow lines. In the AGN unification model (e.g. Antonucci 1993), type 1 AGNs are viewed face-on with the broad-line region (BLR) visible to the observer, while type 2 AGNs are viewed edge-on with the broad-line region blocked by a putative dusty torus. The sub-classes (e.g., type 1.5, 1.8, and 1.9) are also introduced (see Osterbrock & Koski 1976; Osterbrock 1981) based on the emission-line width and relative strength of the broad-line to the narrow-line. There are broad $H\alpha$ line and very weak or undetectable broad $H\beta$ line in type 1.9, broad $H\alpha$ line and weak broad $H\beta$ line in type 1.8 (see Cohen et al. 1986), and comparable $H\alpha$ and $H\beta$ lines in type 1.5.

In recent years, several tens of so-called changing-look AGNs (CL-AGNs hereafter) have been discovered, which show disappearance/appearance of broad emission lines within a timescale of decades or years (e.g. Denney et al. 2014; Shappee et al. 2014; LaMassa et al. 2015; McElroy et al. 2016; Parker et al. 2016; Ruan et al. 2016; Yang et al. 2018; Raimundo et al. 2019; Graham et al. 2020; Ai et al. 2020; Wang et al. 2020; Kollatschny et al. 2020), or even months (e.g. Katebi et al. 2019; Trakhtenbrot et al. 2019). The term “changing-look” was originally used to describe the changes of

AGNs from Compton-thick to Compton-thin (or vice versa) based on the X-ray observations (e.g. Matt et al. 2003). In this paper, the term “changing-look” refers to the change in optical emission lines. The physical mechanism of the changing-look phenomena is still under debate. On the one hand, the “changing-look” can be attributed to variable obscuration, such as obscuring material moving in or out from our line of sight (e.g. Marin et al. 2013; Agís-González et al. 2014; Rivers et al. 2015; Turner et al. 2018), where the intrinsic emission is roughly unchanged. On the other hand, the changing-look may associate with the variation of intrinsic radiation (e.g., the change of accretion disk Penston & Perez 1984; Elitzur et al. 2014). Correlated variability in the X-ray (e.g. Parker et al. 2016, 2019; Ricci et al. 2020), the optical/UV (e.g. Dexter et al. 2019) and the infrared band (e.g. Sheng et al. 2017; Stern et al. 2018) with the AGN type change supports variable accretion as the physical origin in some CL-AGNs, which is also supported by that the absorption is roughly unchanged in some CL-AGNs (e.g. Husemann et al. 2016; Ai et al. 2020; Wang et al. 2020).

The Seyfert galaxy Mrk 1018 at $z = 0.042$ has undergone a full cycle with twice types transitions during the past 40 years. It transitioned from type 1.9 to type 1 between 1979 and 1984 (Cohen et al. 1986) and returned to type 1.9 after 30 years (see McElroy et al. 2016; Husemann et al. 2016; Krumpel et al. 2017). The optical spectroscopic observations reveal that Mrk 1018 is a type 1 AGN in 2010 December and a type 1.9 AGN in 2015 January (McElroy et al. 2016; Kim et al. 2018). The optical spectroscopic observation of Mrk 1018 in 2019 October shows a faint broad $H\beta$ line component in

* E-mail: qwwu@hust.edu.cn

Hutsemékers et al. (2020), which is similar to the type 1.9 spectrum as reported in McElroy et al. (2016).

In this work, we explore the possible physical mechanism for the changing look by performing an extensive data analysis for a CL-AGN of Mrk 1018 in the radio, the optical/UV, and the X-ray bands. We mainly focus on the period of 2005–2019, which is covered by multi-wavelength observations. According to the optical spectroscopic results, we identify that the period of 2005–2010 is the type 1 AGN phase, and 2015–2019 is the type 1.9 AGN phase. The paper is organized as follows. In Section 2, we describe the observations and the data reduction in different wavebands. In Section 3, we present the multi-wavelength observational results. In Section 4, we discuss possible physics behind the observational results. Finally, we summarize our results in Section 5. Throughout this work, we use a flat Λ -CDM cosmological model with $\Omega_M=0.27$, $\Omega_\Lambda=0.73$ and a Hubble constant of $70 \text{ km s}^{-1} \text{ Mpc}^{-1}$. We adopt the luminosity distance $d_L = 176 \text{ Mpc}$ and the black hole (BH) mass measurement $\log(M_{\text{BH}}/M_\odot) = 7.84$ (Ezhikode et al. 2017; Noda & Done 2018) for Mrk 1018.

2 DATA REDUCTION AND ANALYSIS

2.1 X-ray data analysis

We analyse the public archival data of *Swift*, *XMM-Newton*, *Chandra* and *NuSTAR* during the period between 2005 and 2019. We use the cosmic abundances of Wilms et al. (2000) and the photoelectric absorption cross sections from Verner & Yakovlev (1995). All the X-ray spectra are fitted by an absorbed power-law model `tbabs*zpowerlw` with the absorption by the Galactic hydrogen fixed at $N_{\text{HI,Gal}} = 2.43 \times 10^{20} \text{ cm}^{-2}$ (Kalberla et al. 2005) since no intrinsic absorption beyond Galactic is detected (see Husemann et al. 2016; Krumpe et al. 2017). The 2–10 keV flux are calculated by *cfux* component within XSPEC (v12.10). The observation information and best-fitting parameters including photon index (Γ), unabsorbed flux in 2–10 keV ($F_{2-10 \text{ keV}}$) are listed in Table A1. The long-term X-ray light curve in 2–10 keV band is shown in the top panel of Figure 1.

2.1.1 *Swift*/XRT

The X-ray telescope (XRT) on board *Swift* has the highest cadence monitoring observations of Mrk 1018 in the X-ray band, especially after 2015. We reprocess the archive data of *Swift*/XRT observations performed in photon counting mode with XRTPIPELINE. The source region is a circle centered at the nucleus of Mrk 1018, the radius of which is determined by the count rate of each observation according to Evans et al. (2009). We use XSELECT to extract the source and background spectra. The spectra are grouped by the a minimum of one count per bin. The XRT spectra of Mrk 1018 in the 0.5–10 keV range are fitted using the Bayesian X-ray Analysis software BXA¹ (Buchner et al. 2014) which connects the nested sampling algorithm UltraNest (Buchner 2021).

2.1.2 *Chandra*/ACIS-S

We extract the ACIS-S spectra with CIAO (v4.12) and CALDB (v4.9.1). For the observation in November of 2010 (ObsID 12868),

which is affected by the pile-up effect, we adopt the fitting results from Husemann et al. (2016) which excluded the bright pixels and corrected the photon loss for this observation. The other observations are extracted from a $3''$ radius circle and the background spectra are extracted from an annulus with $5''$ inner radius and $15''$ outer radius (see also LaMassa et al. 2017). Then the spectra are grouped by a minimum of 20 counts per bin and fitted in the 0.5–8 keV range.

2.1.3 *XMM-Newton*/EPIC-PN

We analyse the archival data sets of Mrk 1018 derived by the EPIC-PN on board *XMM-Newton*. The source is observed in 2005 (ObsID 201090201) and 2008 (ObsID 554920301). We reduce the PN data with EPPROC in SAS-16.1.0. The source and background regions are a $40''$ and $60''$ radius circle, respectively. Each spectrum is grouped by a minimum of 30 counts per bin and fitted in the 2–10 keV range.

2.1.4 *NuSTAR*

We analyse the archival data sets of Mrk 1018 on board *NuSTAR*, which are reduced through the NUIPELINE task of the NUSTARDAS package. The source region is a $50''$ radius circle at the center of the source, and the background is extracted from the blank region. Each spectrum is grouped by a minimum of 30 counts per bin and fitted in the 3–79 keV range.

2.2 *Swift*/UVOT data analysis

There are six filters in the optical/UV band of *Swift*/UVOT, which are V, B, U, UVW1, UVM2, and UVW2 bands. We use the tool *uvotsource* to do the aperture photometry for each filter of all the observations. The source aperture radius is $5''$ and the background is chosen in a blank region with a much larger radius. According to the results in Noda & Done (2018), the emission of the host galaxy is dominated in the V and the B band, we then discard all the results of the V and the B band.

In order to correct the Galactic extinction, we adopt $E(B-V) = 0.036$ (see Noda & Done 2018) and $R_V = 3.1$ for the Galactic extinction and calculate the values of A_λ for U, UVW1, UVM2, and UVW2 band are 0.18, 0.25, 0.35 and 0.31 assuming the extinction model of Fitzpatrick & Massa (2007). In order to estimate the intrinsic optical/UV flux from the nucleus, we subtract the contribution from the host galaxy, which is estimated from the broadband spectral modeling result in Noda & Done (2018). The results of the long-term optical and UV light curves from *Swift*/UVOT are shown in the middle panel of Figure 1 and listed in Table A2.

2.3 Radio data analysis

We analyse the archival data of Very Large Array (VLA) observations for Mrk 1018 with CASA version 5.3.0 (McMullin et al. 2007). For the reduction of the pre-EVLA upgrade VLA data (VLA, project ID: AU0020, AB0476, AB0540, and AB0878), we manually flag and calibrate the data, then clean the image following the instruction². For the new Karl G. Jansky Very Large Array data (JVLA,

¹ <http://johannesbuchner.github.io/BXA/index.html>

² https://casaguides.nrao.edu/index.php/VLA_5_GHz_continuum_survey_of_Seyfert_galaxies

project ID: 16A-444, 16B-084, and 18B-245), calibrations are performed using script `EVLA_pipeline1.4.2`³. Different bands are split into different MS files after checking the radio frequency interference and calibration. Then the source is imaged using `TCLEAN` method and integrated flux is estimated via `IMFIT` task. The uncertainty of flux density is calculated from $\sigma_S = \sqrt{(rms)^2 + (0.05 \times S)^2}$, where 5% absolute flux error is taken into account, except for the quick look image result in epoch 1 of *VLA Sky Survey (VLASS1.1)*, where 15% system error is considered according to the *VLASS Epoch 1 Quick Look Users Guide*⁴. The imaging results are listed in Table. A3.

To compare between different periods and keep consistent with the radio and X-ray correlation in literature, we convert the radio flux to 5 GHz if it was observed at other wavebands using $S_\nu \propto \nu^{-\alpha_R}$. The radio flux density of Mrk 1018 in the same band varied little before 2015, so we assume the radio spectral index also remains constant during this period. We calculate the $\alpha_{L-X} = 0.3 \pm 0.08$ using the observations on 50970 MJD (X band) and 52490 MJD (L band), then convert the flux densities at other bands to 5 GHz during this period (see Table A3). There is one observation with two bands (C and X) available on MJD 57481, the $\alpha_{C-X} = 0.25 \pm 0.1$ is consistent within uncertainties with previous measured α_{L-X} . We then use this value to convert the flux densities of other bands to 5 GHz after MJD 57481. The estimated radio light curve at 5 GHz after 2005 is present in the bottom panel of Figure 1.

3 RESULTS

3.1 Multi-wavelength light curves

Multi-wavelength light curves of Mrk 1018 are presented in Figure 1. Between 2005 and 2010, when Mrk 1018 stayed in the bright type 1 phase, the X-ray flux was roughly unchanged. The optical/UV flux showed a slight decline by a factor ~ 1.4 during 2005–2007.

Between 2010 and 2015, both the optical/UV and the X-ray flux showed rapid decay (see also McElroy et al. 2016; Husemann et al. 2016), and Mrk 1018 changed from type 1 into type 1.9. The optical/UV and X-ray flux declined by a factor of ~ 17 and ~ 7.5 , respectively.

We find a re-flare (around 2013–2014) during the decay phase, while the amplitude of X-ray variation is higher than those in optical/UV bands (see Figure 1, the X-ray flux increase by a factor ~ 3 within ~ 100 days then decrease by a factor of ~ 4.2 . The optical/UV flux increase by a factor of ~ 1.5 within ~ 100 days then decrease by a factor of ~ 3.8). After 2015, the source went into the faint type 1.9 phase. The X-ray showed stronger variability ($\sim 14\%$) than optical/UV bands ($\sim 6\%$) during the type 1.9 phase in 2018.

The 5 GHz radio flux did not decline during the decay of X-ray and optical/UV emission between 2010 and 2015 and, however, it decreased by $\sim 20\%$ in the type 1.9 phase during 2016–2017 (see Figure 1).

3.2 Time lag between X-ray and UV variations

Between 2018 August and 2018 November, *Swift* executed an intensive monitoring campaign on Mrk 1018 (48 visits within 84 days).

³ <https://science.nrao.edu/facilities/vla/data-processing/pipeline/scripted-pipeline>

⁴ <https://science.nrao.edu/science/surveys/vlass/vlass-epoch-1-quick-look-users-guide>

Table 1. Detected time lag τ of the UV variations behind the X-ray. The X-ray band is taken as the reference. The uncertainties refer to 1σ range.

band	method	τ [day]	correlation coefficient	p -value
U	ICCF	13.4^{+17}_{-6}	0.40	3.8e-3
UVW1	ICCF	$18.1^{+6.5}_{-10.1}$	0.46	1.3e-3
UVM2	ICCF	$21.0^{+8}_{-5.1}$	0.50	1.4e-3
UVW2	ICCF	$21.0^{+6.5}_{-14}$	0.37	1.7e-2

band	method	τ [day]	w range [day]	w [day]
U	JAVELIN	$14.7^{+10.4}_{-8.6}$	0–40	$16.5^{+13.4}_{-10.6}$
UVW1	JAVELIN	$21.4^{+2.2}_{-2.8}$	0–40	$9.3^{+8.2}_{-5.7}$
UVM2	JAVELIN	$23.4^{+7.3}_{-9.6}$	15–40	$25.1^{+8.7}_{-7.2}$
UVW2	JAVELIN	$20.9^{+11.4}_{-13.2}$	0–40	$12.7^{+16.9}_{-10.4}$

In order to examine the correlation between X-ray and UV flux variations during this period, we use the interpolation cross correlation function (ICCF; Peterson et al. 1998; Sun et al. 2018) with a time lag (τ) range of 0–40 days (around half the overlap). The interpolation time step of 1 day are both applied to X-ray and UV light curves. The flux randomization and random subset selection methods are employed with 10000 realizations in the Monte Carlo simulation to estimate the centroid time lag and the uncertainties⁵.

We also use the JAVELIN algorithm (Zu et al. 2011, 2013) to further examine the time lag that we estimate through the ICCF method. The JAVELIN approach fits the light curves using a damped random walk (DRW) model, convolves them with a top-hat transfer function (TF), and aligns them to recover the time lag and other parameters (such as the amplitude and timescale of the DRW process, the height and width (w) of the top-hat transfer function) with the Monte Carlo method. We first restrict the range of time lag τ and the w to be 0–40 days. The measured time lag τ from JAVELIN are consistent with those of ICCF method (see Table 1). However, there are two peaks of the posterior distribution of τ (~ 20 and 32 days) between X-ray and UVM2 band, which does not agree with the ICCF method. We then restrict the range of w to be 15–40 days and perform an additional simulation. Only one peak at ~ 23 days is shown in the posterior distribution of τ , we then take this as the primary time lag between X-ray and UVM2 bands. So both ICCF and JAVELIN methods give consistent time lags between X-ray and U band at ~ 14 days, and time lags between X-ray and UVW1/UVM2/UVW2 at ~ 20 days. The results from the ICCF and JAVELIN methods between X-ray and the four UVOT bands are listed in Table 1 and presented in Figure 2.

3.3 Γ - L_X/L_{Edd} and α_{ox} - L_X/L_{Edd} correlation

We present the Γ -log L_X/L_{Edd} correlation of Mrk 1018 in Figure 3, where only the data of *Swift*/XRT are adopted to avoid the discrepancies of different instruments. We find an evident negative correlation

⁵ The code pyCCF is available in <http://ascl.net/code/v/1868>

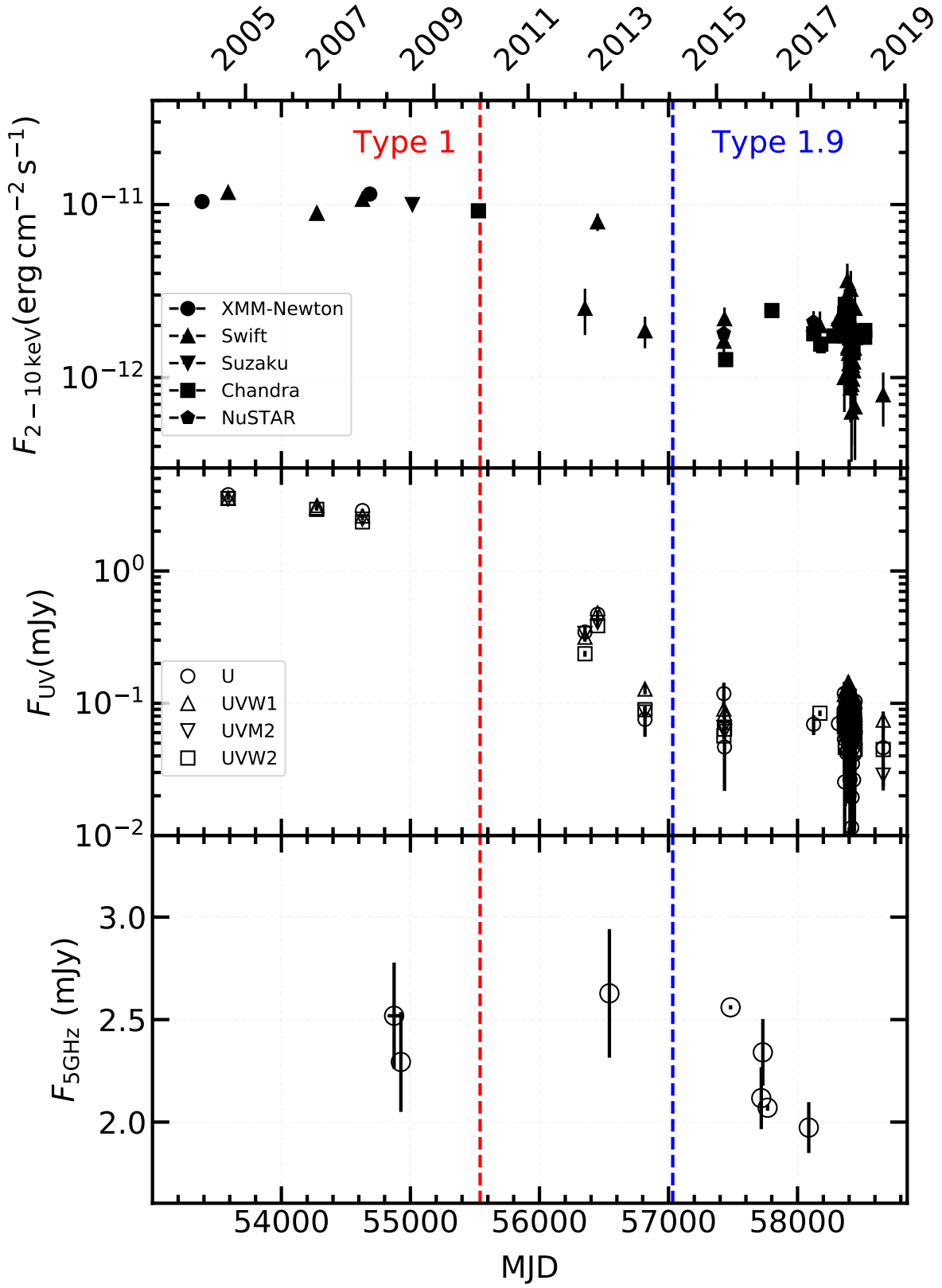


Figure 1. Multi-wavelength light curves of Mrk 1018 between 2005 and 2019. Red and blue vertical dashed lines represent the timeline of optical spectroscopic confirmation at type 1 and type 1.9, respectively. A re-flare during the changing-look phase is found in both the X-ray and the optical/UV bands.

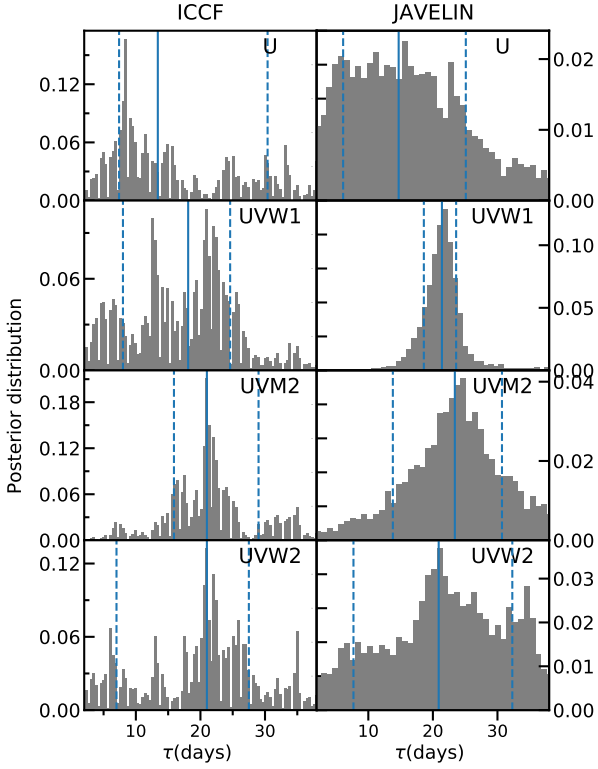


Figure 2. The posterior distribution of τ with ICCF and JAVELIN methods. The solid lines represent the centroid time lag and the dashed lines correspond to 1σ range uncertainties.

between the photon index and the Eddington-scaled X-ray luminosity in the type 1.9 phase, where the Spearman correlation coefficient is -0.63 ($p = 5.1 \times 10^{-7}$). The data in the type 1 phase and the re-flare apparently deviate from the negative correlation (see Figure 3).

The correlation of $\alpha_{\text{OX}} - \log L_X/L_{\text{Edd}}$ is also explored in Figure 4. We calculate the α_{OX} according to the Equation 1. The L_{UVW1} is derived from UVW1 filter of the *Swift*/UVOT with central wavelength 2600\AA and full-width at half max of $\sim 683\text{\AA}$ (Poole et al. 2008). The $L_{2\text{ keV}}$ is calculated according to Equation 2, where the $L_{2-10\text{ keV}}$ and photon index Γ are derived from X-ray spectra fitting.

$$\alpha_{\text{OX}} = \frac{\log(L_{\text{UVW1}}/L_{2\text{keV}})}{\log(\nu_{2\text{keV}}/\nu_{\text{UVW1}})} = 0.384 \times \log(L_{\text{UVW1}}/L_{2\text{keV}}) \quad (1)$$

$$L_{2\text{ keV}} = \begin{cases} \frac{L_{2-10\text{ keV}}(2-\Gamma)}{\nu_{2\text{ keV}} \times (5^{2-\Gamma} - 1)} & , \Gamma \neq 2 \\ \frac{L_{2-10\text{ keV}}}{\nu_{2\text{ keV}} \times \ln 5} & , \Gamma = 2 \end{cases} \quad (2)$$

The α_{OX} and $\log L_X/L_{\text{Edd}}$ also follow a negative correlation in the type 1.9 phase, where the Spearman correlation coefficient is -0.67 ($p = 1.7 \times 10^{-7}$). The data in type 1 phase and the re-flare also apparently deviate from the negative correlation (Figure 4).

3.4 Radio–X-ray luminosity correlation

The correlation of the 5 GHz radio luminosity ($\log L_R$) and 2–10 keV X-ray luminosity ($\log L_X$) is presented in Figure 5, where the quasi-simultaneous radio and X-ray observations within 100

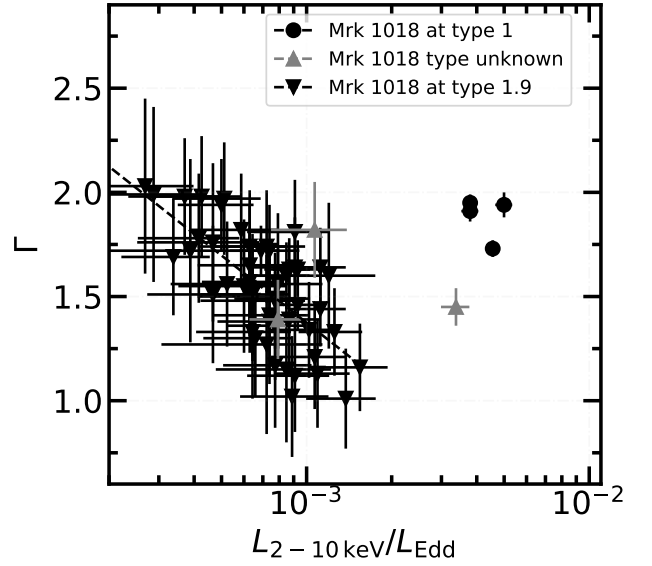


Figure 3. The $\Gamma - L_X/L_{\text{Edd}}$ correlation. Only data of *Swift*/XRT are included here. The dashed line represent the best fitting of the negative correlation in the type 1.9 phase.

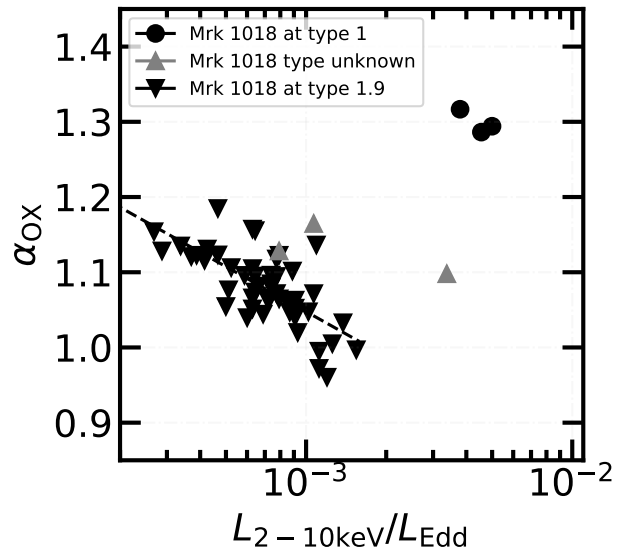


Figure 4. The $\alpha_{\text{OX}} - L_X/L_{\text{Edd}}$ correlation. The dashed line represent the best fitting of the negative correlation in the type 1.9 phase.

days are adopted. The radio and X-ray luminosity follow a quite flat correlation during the luminosity range of $L_X/L_{\text{Edd}} \sim 5 \times 10^{-4} - 4 \times 10^{-3}$, where the Spearman correlation coefficient is 0.2 ($p = 0.75$). Coincidentally, the two points in 2017 and average of the $\log L_R$ and $\log L_X$ correlation of Mrk 1018 roughly follows the fundamental plane defined by the sample of AGN and XRB (e.g. Plotkin et al. 2012). But the points before 2016 deviate the fundamental plane where $L_R \propto L_X^{0.6}$.

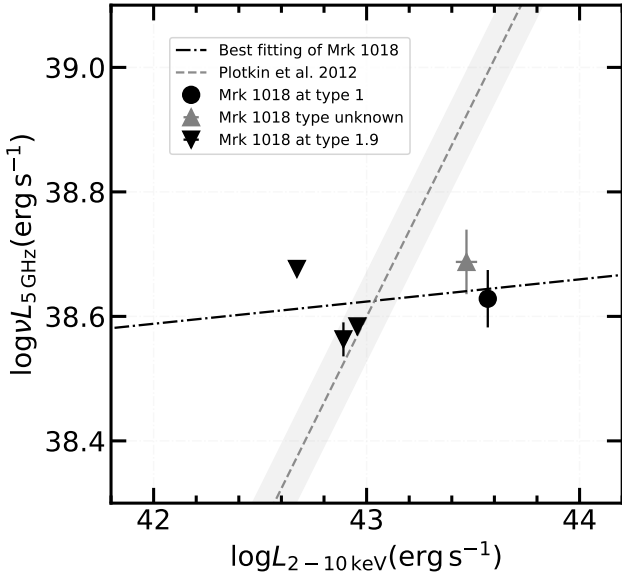


Figure 5. The $\log L_R$ - $\log L_X$ correlation. The dash-dot line represents the best-fitting line of Mrk 1018 with a slope of ~ 0.04 . The fundamental plane of a sample of black holes in Plotkin et al. (2012) with a slope of ~ 0.6 is presented in the grey dashed line with intrinsic $\sigma = 0.07$ for comparison.

4 DISCUSSION

4.1 The spectral evolution and possible accretion mode transition

The X-ray photon index can shed light on the physical properties of the hot plasma in the advection-dominated accretion flow (ADAF) or corona above and below the cold disk, which is controlled mainly by the electron temperature and optical depth. The negative/positive correlation of Γ - $\log L_X/L_{\text{Edd}}$ below/above a critical value ($L_X/L_{\text{Edd}} \sim 10^{-3}$) has been reported in both AGNs and X-ray binaries (XRBs) (e.g. Wu & Gu 2008; Gu & Cao 2009; Younes et al. 2011; Yang et al. 2015; Yan et al. 2020). The reason for the opposite X-ray spectral behavior is thought to be the differences of the seed photons for the Compton scattering, i.e. the seed photons are from the synchrotron emission of the hot ADAF at the lower luminosity branch, while from the thermal emission from Shakura–Sunyaev disk (SSD; e.g. Qiao & Liu 2013) at the higher luminosity branch. There is an evident negative correlation of Γ - $\log L_X/L_{\text{Edd}}$ in the type 1.9 phase of Mrk 1018, which is similar to the low-luminosity AGNs and the low/hard state XRBs. The data in the type 1 phase deviate from the negative correlation evidently, where the physical origin for optical and X-ray emission should be changed.

The optical/UV-to-X-ray spectral index α_{ox} is a good indicator of the broadband spectral energy distribution (SED), where the optical/UV and X-ray emission come from the cold SSD (or outer truncated SSD) and hot corona/ADAF respectively in AGNs. The negative and positive correlations of α_{ox} - $\log L_X/L_{\text{Edd}}$ have been found in low-luminosity AGNs (e.g. Xu 2011; Li & Xie 2017) and luminous AGNs (e.g. Lusso et al. 2010; Vagnetti et al. 2013; Lusso & Risaliti 2016). The ADAF model can roughly explain the negative $\alpha_{\text{ox}}-L_{\text{bol}}$ correlation at the lower luminosity branch (Xu 2011; Li & Xie 2017), and the disk-corona model can explain the positive $\alpha_{\text{ox}}-L_{\text{bol}}$ correlation at the higher luminosity branch (Lusso & Risaliti 2017; Kubota & Done 2018; Arcodia et al. 2019).

Sobolewska et al. (2011) simulated the spectral states of AGNs by analogy with BHXRBs and found that the simulated AGNs at different spectral states and luminosity roughly follow a “V”-shape $\alpha_{\text{ox}}-L_{\text{bol}}$ correlation (negative/positive correlation below/above a critical value, see also in Ruan et al. 2019b). In other words, the opposite correlations between α_{ox} and L also support the idea that the accretion mode changes in the high and low luminosity AGNs (see Sobolewska et al. 2011; Ruan et al. 2019b). There is an evident negative correlation of $\alpha_{\text{ox}}-\log L_X/L_{\text{Edd}}$ in the type 1.9 AGN phase of Mrk 1018, which is similar to the low-luminosity AGNs. The data in type 1 phase apparently deviate from the negative correlation, which indicates that the accretion mode is different from type 1.9 phase. A much stronger SSD component in type 1 phase will lead to a higher α_{ox} .

The evolutions of both Γ - $\log L_X/L_{\text{Edd}}$ and $\alpha_{\text{ox}}-\log L_X/L_{\text{Edd}}$ suggest that the strong evolution of underlying accretion disk in Mrk 1018 during the type transition. The change of the broad emission lines is most possibly regulated by the appearance or disappearance of cold disk near the black hole horizon, which regulates the radiative efficiency of accretion flow and/or ionization luminosity for the clouds in broad line region.

4.2 The variability timescale

In Mrk 1018, the broadband spectra are dramatically changed with the rapid decay of luminosity (see also Husemann et al. 2016; Noda & Done 2018) between 2010 and 2015. More and more studies show that the spectral evolution of CL-AGNs somehow are quite similar to the spectral state transitions in Galactic BH XRBs (Noda & Done 2018; Ruan et al. 2019a,b; Liu et al. 2020). The state transitions in BHXRBs normally occur on timescale of days to tens of days (Yu & Yan 2009; Dunn et al. 2010), which is usually attributed to the viscous timescale of the inner disk in the truncated accretion disk model (see reviews in Done et al. 2007). The viscous timescale τ_{vis} for a $10^8 M_{\odot}$ AGN is given by,

$$\tau_{\text{vis}} \sim 5.7 \times 10^{-3} \alpha^{-1} \left(\frac{M_{\text{BH}}}{10^8 M_{\odot}} \right) \left(\frac{R_{\text{tr}}}{R_g} \right)^{3/2} \left(\frac{H}{R} \right)^{-2} \text{ days} \quad (3)$$

The H/R is the ratio between disk height and disk radius, the R_{tr} is the inner truncated radius. So if the truncated radius of the accretion disk is smaller than $\sim 20R_g$, the viscous timescale will roughly agree with the spectral evolution timescale ($\lesssim 5$ years) of Mrk 1018 for $\alpha = 0.1$ and $H/R = 0.05$ (e.g. Liu et al. 2020). Such a viscous timescale is too short for a standard disk, since the required H/R is much larger than that expected in standard disk. So there are also some different scenarios proposed to account for such a short timescale, such as the thermal and heating/cooling front timescales in the innermost regions of the accretion disk (Stern et al. 2018), a radiation-pressure dominated accretion disk with faster sound speed and hence the viscous speed (Noda & Done 2018), a thick disk supported by the magnetic pressure (Dexter & Begelman 2019), and the radiation pressure instability and transition between standard disk and ADAF (Snigowska et al. 2020).

A re-flare with a timescale on a magnitude of hundreds of days during the decay phase was found, where the physical reason for the variability is unclear. The rise timescale ($\lesssim 100$ days) of the re-flare is consistent with the thermal timescale at an emission distance of $R \lesssim 200R_g$. A short “turn-on” (appearance of broad emission lines and increasing luminosity by a factor of 8) timescale ~ 70 days of PS1-13cbe is also suggested to be compatible with the thermal timescale under the scenario of UV/X-ray reprocessing (Katebi et al. 2019). However, there is no information about the

emission lines of Mrk 1018 during the re-flare, so we have no idea whether the AGN type has been changed during this re-flare.

We estimated the time lag $\tau \sim 20$ days between UV and X-ray variations of Mrk 1018 in the type 1.9 phase, which is much longer than previous results in other nearby AGNs (usually less than 5 days, e.g. Arévalo et al. 2009; Shappee et al. 2014; Buisson et al. 2017; Edelson et al. 2017, 2019; Lobban et al. 2020). The X-ray reprocessing is usually thought to be the main mechanism for the optical/UV variation (e.g. Krolik et al. 1991; Cackett et al. 2007; Kammoun et al. 2021), where the optical/UV flux is expected to vary in response to X-ray after a light-crossing time. In the X-ray reprocessing scenario (Cackett et al. 2007), the time delay is expected to be positively correlated with the wavelength, which is not found in Mrk 1018 (see Table 1). The time lag ~ 20 days corresponds to a light-crossing size $\sim 5000 R_g$ for Mrk 1018, which is also much larger than the typical disk size of AGNs. Such a long UV/X-ray time lag is approximately consistent with the thermal timescale at $R \sim 65R_g$ for Mrk 1018, which may suggest a slower physical process, such as the thermal fluctuation or instability (Kelly et al. 2009; Gardner & Done 2017).

4.3 Radio–X-ray correlation

The simultaneous X-ray and radio emission track the connection between accretion and ejection activities of CL-AGNs (e.g. Koay et al. 2016; Yang et al. 2021). It is widely accepted that there is a non-linear correlation between the 5 GHz radio luminosity and the 2–10 keV X-ray luminosity spanning from the super-massive black holes to stellar mass black holes: $L_R \propto L_X^{0.6}$ (e.g. Merloni et al. 2003; Falcke et al. 2004). There are also some sources following a steeper radio–X-ray correlation with a power-law index of ~ 1.4 at higher luminosity, a flat radio–X-ray correlation with a power-law index of ~ 0 at transition stage (e.g. Coriat et al. 2011; Cao et al. 2014; Xie et al. 2016). The “hybrid” radio–X-ray correlation is possibly regulated by the underlying accretion processes (e.g. Xie & Yuan 2016) or due to different jet properties (e.g. Islam & Zdziarski 2018; Espinasse & Fender 2018). It should be noted that Mrk 1018 roughly follows the radio–X-ray correlation as defined by other BH sources (Plotkin et al. 2012) even though its own correlation is quite flat. The X-ray luminosity’s decline by a factor ~ 7.5 requires a variability by a factor of ~ 3.3 in radio luminosity to follow the radio–X-ray correlation with a slope of 0.6, which is far beyond the radio variability of Mrk 1018. The possible physical reasons include: 1) the radio variability timescale is much longer than X-ray since that the radio emission comes from a larger scale of jet; 2) the flat radio–X-ray correlation is mainly regulated by the X-ray emission, where the accretion rate does not vary much but the radiative efficiency change a lot when the accretion rate is close to a critical value. The Eddington ratio of bolometric luminosity is around 1% (Noda & Done 2018), which suggests that the radiative efficiency in Mrk 1018 may indeed easily suffer strong variations due to the transition of accretion modes.

5 SUMMARY

The main results are summarized as follows,

(i) We present the long-term and multi-wavelength variability from radio to X-ray band for a CL-AGN of Mrk 1018. We find a re-flare in both optical/UV and X-ray bands during the decay phase and a time lag ~ 20 days of optical/UV behind X-ray variations during the type 1.9 phase.

(ii) We find negative correlations of $\Gamma-L_X/L_{\text{Edd}}$ and $\alpha_{\text{ox}}-L_X/L_{\text{Edd}}$ in the type 1.9 phase, which are consistent with the prediction of the radiatively inefficient accretion (e.g., ADAF). The data in the type 1 phase deviate from the negative correlations, where the accretion mode may change into a radiatively efficient disk-corona system. Therefore, the change of broad emission lines might be regulated by the underlying accretion process.

(iii) The radio emission in CL-AGN of Mrk 1018 was roughly unchanged before the type 1.9 phase (2005–2015), then it slightly declined about $\sim 20\%$ during 2016–2017. Therefore, radio–X-ray correlation is quite flat in Mrk 1018, which is much shallower than that found in low-luminosity AGNs and low-hard state XRBs with a slope of ~ 0.6 .

ACKNOWLEDGEMENTS

We thank the anonymous referee for useful comments and suggestions. We thank Prof Minfeng Gu for the discussions on the radio observations of CL-AGNs and Dr Linhui Wu and Minhua Zhou for discussions on the VLA data reduction. B.L. and Q.W. are supported in part by the NSFC (grant U1931203); Z.Y. is supported in part by the Natural Science Foundation of China (grants 11773055, U1938114), the Youth Innovation Promotion Association of CAS (ids. 2020265); W.Y. would like to acknowledge the support in part by the National Program on Key Research and Development Project (Grant No.2016YFA0400804) and the National Natural Science Foundation of China (grant number 11333005 and U1838203).

DATA AVAILABILITY

The data underlying this article are available through HEASARC Browse database and NRAO Science Data Archive.

REFERENCES

- Agís-González B., et al., 2014, *MNRAS*, **443**, 2862
 Ai Y., et al., 2020, *ApJ*, **890**, L29
 Antonucci R., 1993, *Annual Review of Astronomy and Astrophysics*, **31**, 473
 Arcodia R., Merloni A., Nandra K., Ponti G., 2019, *A&A*, **628**, A135
 Arévalo P., Uttley P., Lira P., Breedt E., McHardy I. M., Churazov E., 2009, *MNRAS*, **397**, 2004
 Becker R. H., Helfand D. J., White R. L., Gregg M. D., Laurent-Muehleisen S. A., 2003, *VizieR Online Data Catalog*, p. VIII/71
 Becker R. H., Helfand D. J., White R. L., Gregg M. D., Laurent-Muehleisen S. A., 2012, *VizieR Online Data Catalog*, p. VIII/90
 Buchner J., 2021, *The Journal of Open Source Software*, **6**, 3001
 Buchner J., et al., 2014, *A&A*, **564**, A125
 Buisson D. J. K., Lohfink A. M., Alston W. N., Fabian A. C., 2017, *MNRAS*, **464**, 3194
 Cackett E. M., Horne K., Winkler H., 2007, *MNRAS*, **380**, 669
 Cao X.-F., Wu Q., Dong A.-J., 2014, *ApJ*, **788**, 52
 Cohen R. D., Rudy R. J., Puetter R. C., Ake T. B., Foltz C. B., 1986, *The Astrophysical Journal*, **311**, 135
 Condon J. J., Cotton W. D., Greisen E. W., Yin Q. F., Perley R. A., Taylor G. B., Broderick J. J., 1998, *AJ*, **115**, 1693
 Condon J. J., Cotton W. D., Broderick J. J., 2002, *The Astronomical Journal*, **124**, 675
 Coriat M., et al., 2011, *MNRAS*, **414**, 677
 Denney K. D., et al., 2014, *ApJ*, **796**, 134
 Dexter J., Begelman M. C., 2019, *MNRAS*, **483**, L17

- Dexter J., et al., 2019, *ApJ*, **885**, 44
- Done C., Gierliński M., Kubota A., 2007, *A&ARv*, **15**, 1
- Dunn R. J. H., Fender R. P., Körding E. G., Belloni T., Cabanac C., 2010, *MNRAS*, **403**, 61
- Edelson R., et al., 2017, *ApJ*, **840**, 41
- Edelson R., et al., 2019, *ApJ*, **870**, 123
- Elitzur M., Ho L. C., Trump J. R., 2014, *MNRAS*, **438**, 3340
- Espinasse M., Fender R., 2018, *MNRAS*, **473**, 4122
- Evans P. A., et al., 2009, *MNRAS*, **397**, 1177
- Ezhikode S. H., Gandhi P., Done C., Ward M., Dewangan G. C., Misra R., Philip N. S., 2017, *Monthly Notices of the Royal Astronomical Society*, **472**, 3492
- Falcke H., Körding E., Markoff S., 2004, *A&A*, **414**, 895
- Fitzpatrick E. L., Massa D., 2007, *ApJ*, **663**, 320
- Gardner E., Done C., 2017, *MNRAS*, **470**, 3591
- Graham M. J., et al., 2020, *MNRAS*, **491**, 4925
- Gu M., Cao X., 2009, *MNRAS*, **399**, 349
- Heywood I., et al., 2016, *MNRAS*, **460**, 4433
- Hodge J. A., Becker R. H., White R. L., Richards G. T., Zeimann G. R., 2011, *The Astronomical Journal*, **142**, 3
- Husemann B., et al., 2016, *Astronomy and Astrophysics*, **593**, L9
- Hutsemékers D., Agís González B., Marin F., Sluse D., 2020, *A&A*, **644**, L5
- Islam N., Zdziarski A. A., 2018, *MNRAS*, **481**, 4513
- Kalberla P. M. W., Burton W. B., Hartmann D., Arnal E. M., Bajaja E., Morras R., Pöppel W. G. L., 2005, *A&A*, **440**, 775
- Kammoun E. S., Papadakis I. E., Dovčiak M., 2021, *MNRAS*, **503**, 4163
- Katebi R., et al., 2019, *MNRAS*, **487**, 4057
- Kelly B. C., Bechtold J., Siemiginowska A., 2009, *ApJ*, **698**, 895
- Kim D. C., Yoon I., Evans A. S., 2018, *The Astrophysical Journal*, **861**, 51
- Koay J. Y., Vestergaard M., Bignall H. E., Reynolds C., Peterson B. M., 2016, *MNRAS*, **460**, 304
- Kollatschny W., et al., 2020, *A&A*, **638**, A91
- Krolik J. H., Horne K., Kallman T. R., Malkan M. A., Edelson R. A., Kriss G. A., 1991, *ApJ*, **371**, 541
- Krumpe M., et al., 2017, *Astronomy and Astrophysics*, **607**, L9
- Kubota A., Done C., 2018, *MNRAS*, **480**, 1247
- LaMassa S. M., et al., 2015, *ApJ*, **800**, 144
- LaMassa S. M., Yaqoob T., Kilgard R., 2017, *The Astrophysical Journal*, **840**, 11
- Li S.-L., Xie F.-G., 2017, *MNRAS*, **471**, 2848
- Liu Z., Liu H.-Y., Cheng H., Qiao E., Yuan W., 2020, *MNRAS*, **492**, 2335
- Lobban A. P., et al., 2020, *MNRAS*, **494**, 1165
- Lusso E., Risaliti G., 2016, *ApJ*, **819**, 154
- Lusso E., Risaliti G., 2017, *A&A*, **602**, A79
- Lusso E., et al., 2010, *A&A*, **512**, A34
- Marin F., Porquet D., Goosmann R. W., Dovčiak M., Muleri F., Grosso N., Karas V., 2013, *MNRAS*, **436**, 1615
- Matt G., Guainazzi M., Maiolino R., 2003, *MNRAS*, **342**, 422
- McElroy R. E., et al., 2016, *Astronomy and Astrophysics*, **593**, L8
- McMullin J. P., Waters B., Schiebel D., Young W., Golap K., 2007, in Shaw R. A., Hill F., Bell D. J., eds, *Astronomical Society of the Pacific Conference Series Vol. 376, Astronomical Data Analysis Software and Systems XVI*. p. 127
- Merloni A., Heinz S., di Matteo T., 2003, *MNRAS*, **345**, 1057
- Noda H., Done C., 2018, *Monthly Notices of the Royal Astronomical Society*, **480**, 3898
- Osterbrock D. E., 1981, *The Astrophysical Journal*, **249**, 462
- Osterbrock D. E., Koski A. T., 1976, *Monthly Notices of the Royal Astronomical Society*, **176**, 61P
- Parker M. L., et al., 2016, *MNRAS*, **461**, 1927
- Parker M. L., et al., 2019, *MNRAS*, **483**, L88
- Penston M. V., Perez E., 1984, *MNRAS*, **211**, 33P
- Peterson B. M., Wanders I., Horne K., Collier S., Alexander T., Kaspi S., Maoz D., 1998, *PASP*, **110**, 660
- Plotkin R. M., Markoff S., Kelly B. C., Körding E., Anderson S. F., 2012, *MNRAS*, **419**, 267
- Poole T. S., et al., 2008, *MNRAS*, **383**, 627
- Qiao E., Liu B. F., 2013, *ApJ*, **764**, 2
- Raimundo S. I., Vestergaard M., Koay J. Y., Lawther D., Casasola V., Peterson B. M., 2019, *MNRAS*, **486**, 123
- Ricci C., et al., 2020, *ApJ*, **898**, L1
- Rivers E., et al., 2015, *ApJ*, **815**, 55
- Ruan J. J., et al., 2016, *ApJ*, **826**, 188
- Ruan J. J., Anderson S. F., Eracleous M., Green P. J., Haggard D., MacLeod C. L., Runnoe J. C., Sobolewska M. A., 2019a, arXiv e-prints, p. arXiv:1909.04676
- Ruan J. J., Anderson S. F., Eracleous M., Green P. J., Haggard D., MacLeod C. L., Runnoe J. C., Sobolewska M. A., 2019b, *ApJ*, **883**, 76
- Shappee B. J., et al., 2014, *ApJ*, **788**, 48
- Sheng Z., Wang T., Jiang N., Yang C., Yan L., Dou L., Peng B., 2017, *The Astrophysical Journal*, **846**, L7
- Sniegowska M., Czerny B., Bon E., Bon N., 2020, *A&A*, **641**, A167
- Sobolewska M. A., Siemiginowska A., Gierliński M., 2011, *MNRAS*, **413**, 2259
- Stern D., et al., 2018, *ApJ*, **864**, 27
- Sun M., Grier C. J., Peterson B. M., 2018, PyCCF: Python Cross Correlation Function for reverberation mapping studies (ascl:1805.032)
- Trakhtenbrot B., et al., 2019, *ApJ*, **883**, 94
- Turner T. J., Reeves J. N., Braito V., Lobban A., Kraemer S., Miller L., 2018, *MNRAS*, **481**, 2470
- Vagnetti F., Antonucci M., Trevese D., 2013, *A&A*, **550**, A71
- Verner D. A., Yakovlev D. G., 1995, *A&AS*, **109**, 125
- Wang J., Xu D. W., Wei J. Y., 2020, *ApJ*, **901**, 1
- Wilms J., Allen A., McCray R., 2000, *ApJ*, **542**, 914
- Winter L. M., Veilleux S., McKernan B., Kallman T. R., 2012, *ApJ*, **745**, 107
- Wu Q., Gu M., 2008, *ApJ*, **682**, 212
- Xie F.-G., Yuan F., 2016, *MNRAS*, **456**, 4377
- Xie F.-G., Zdziarski A. A., Ma R., Yang Q.-X., 2016, *MNRAS*, **463**, 2287
- Xu Y.-D., 2011, *ApJ*, **739**, 64
- Yan Z., Xie F.-G., Zhang W., 2020, *ApJ*, **889**, L18
- Yang Q.-X., Xie F.-G., Yuan F., Zdziarski A. A., Gierliński M., Ho L. C., Yu Z., 2015, *MNRAS*, **447**, 1692
- Yang Q., et al., 2018, *ApJ*, **862**, 109
- Yang J., et al., 2021, *MNRAS*,
- Younes G., Porquet D., Sabra B., Reeves J. N., 2011, *A&A*, **530**, A149
- Yu W., Yan Z., 2009, *ApJ*, **701**, 1940
- Zu Y., Kochanek C. S., Peterson B. M., 2011, *ApJ*, **735**, 80
- Zu Y., Kochanek C. S., Kozłowski S., Udalski A., 2013, *ApJ*, **765**, 106

This paper has been typeset from a $\text{\TeX}/\text{\LaTeX}$ file prepared by the author.

APPENDIX A: APPENDIX

Table A1: X-ray data of Mrk 1018. Columns include the date of observations, observation ID, the telescope, the photon index Γ with 90% uncertainty, and Galactic-absorption corrected 2–10 keV X-ray flux.

Date (MJD)	ObsID	Telescope	Γ	$F_{2-10 \text{ keV}}$ [$10^{-12} \text{ erg cm}^{-2} \text{ s}^{-1}$]
53385	201090201	X	1.68 ± 0.11	10.40 ± 0.50
53587	35166001	S	1.94 ± 0.06	11.75 ± 0.81
54273	30955002	S	1.91 ± 0.05	8.91 ± 0.62
54275	30955003	S	1.95 ± 0.04	8.91 ± 0.41
54628	35776001	S	1.73 ± 0.04	10.72 ± 0.49
54685	554920301	X	1.79 ± 0.03	11.50 ± 0.20
55015	704044010 ^a	Su	2.00 ± 0.03	10.00 ± 0.50
55527	12868 ^b	C	1.68 ± 0.04	9.20 ± 0.20
56352	49654001	S	1.82 ± 0.23	2.51 ± 0.75
56450	49654002	S	1.45 ± 0.09	7.94 ± 0.91
56817	49654004	S	1.39 ± 0.19	1.86 ± 0.39
57428	60160087002	N	1.85 ± 0.08	1.80 ± 0.10
57429	80898001	S	1.72 ± 0.12	1.62 ± 0.26
57434	80898002	S	1.46 ± 0.12	2.19 ± 0.35
57443	18789	C	1.68 ± 0.03	1.27 ± 0.03
57801	19560	C	1.61 ± 0.02	2.44 ± 0.02
58123	60301022002	N	1.80 ± 0.06	2.10 ± 0.10
58124	88207001	S	1.63 ± 0.15	2.04 ± 0.38
58126	20366	C	1.60 ± 0.03	1.79 ± 0.04
58173	88207002	S	1.60 ± 0.16	2.00 ± 0.41
58180	20367	C	1.63 ± 0.04	1.56 ± 0.03
58182	60301022003	N	1.80 ± 0.06	1.50 ± 0.07
58281	20368	C	1.64 ± 0.03	1.74 ± 0.04
58316	60301022005	N	1.74 ± 0.05	2.00 ± 0.09
58316	88207003	S	1.63 ± 0.14	2.19 ± 0.40
58362	35776002	S	1.98 ± 0.29	1.00 ± 0.37
58363	35776003	S	1.41 ± 0.29	1.74 ± 0.64
58364	35776004	S	1.34 ± 0.23	2.40 ± 0.66
58365	35776005	S	1.48 ± 0.23	1.82 ± 0.50
58368	35776006	S	1.44 ± 0.18	2.63 ± 0.61
58369	35776007	S	1.64 ± 0.19	2.63 ± 0.61
58370	20369	C	1.63 ± 0.03	2.65 ± 0.06
58370	35776008	S	1.81 ± 0.25	2.14 ± 0.69
58374	35776010	S	1.56 ± 0.34	1.86 ± 0.81
58375	35776011	S	1.39 ± 0.23	2.04 ± 0.56
58378	35776014	S	1.33 ± 0.21	2.95 ± 0.75
58384	35776015	S	1.60 ± 0.35	2.82 ± 1.30
58385	35776016	S	1.16 ± 0.21	3.63 ± 0.92
58390	35776017	S	1.49 ± 0.24	1.86 ± 0.56
58390	35776018	S	1.72 ± 0.22	1.74 ± 0.48
58391	35776019	S	1.51 ± 0.29	1.51 ± 0.52
58392	35776020	S	1.50 ± 0.27	1.48 ± 0.51
58393	35776021	S	1.13 ± 0.26	2.57 ± 0.77
58395	35776023	S	1.74 ± 0.27	1.48 ± 0.51
58396	35776024	S	1.82 ± 0.27	1.38 ± 0.48
58399	35776026	S	1.64 ± 0.24	2.14 ± 0.64
58399	35776027	S	1.97 ± 0.27	1.20 ± 0.42
58402	35776029	S	1.74 ± 0.27	1.70 ± 0.63
58409	35776032	S	1.02 ± 0.29	2.09 ± 0.72
58410	35776033	S	1.98 ± 0.28	0.87 ± 0.32
58412	35776034	S	1.01 ± 0.24	3.24 ± 0.89
58413	35776035	S	1.36 ± 0.26	1.82 ± 0.59
58417	35776036	S	1.12 ± 0.27	2.14 ± 0.69
58418	35776037	S	2.03 ± 0.42	0.63 ± 0.31
58420	35776038	S	1.72 ± 0.44	0.91 ± 0.50
58420	35776039	S	1.33 ± 0.32	1.51 ± 0.56
58422	35776040	S	1.30 ± 0.28	1.55 ± 0.53
58423	35776041	S	1.55 ± 0.32	1.41 ± 0.59
58424	35776042	S	1.94 ± 0.22	1.17 ± 0.35
58425	35776043	S	1.78 ± 0.31	0.98 ± 0.38

The superscripts ^(a) and ^(b) represent the fitting results from Winter et al. (2012) and Husemann et al. (2016), respectively.

Table A1 – continued from previous page

Date (MJD)	ObsID	Telescope	Γ	$F_{2-10 \text{ keV}}$ [$10^{-12} \text{ erg cm}^{-2} \text{ s}^{-1}$]
58426	35776044	S	1.15 ± 0.35	2.00 ± 0.87
58427	35776045	S	1.51 ± 0.33	1.10 ± 0.45
58428	35776046	S	1.48 ± 0.29	1.51 ± 0.52
58429	35776047	S	1.38 ± 0.30	1.74 ± 0.60
58430	20370	C	1.64 ± 0.04	1.39 ± 0.03
58433	35776049	S	1.76 ± 0.38	1.10 ± 0.50
58434	35776050	S	1.56 ± 0.30	1.23 ± 0.45
58436	35776051	S	1.57 ± 0.26	1.48 ± 0.48
58437	35776052	S	1.17 ± 0.30	1.82 ± 0.63
58439	35776054	S	1.65 ± 0.29	1.48 ± 0.51
58444	35776056	S	1.21 ± 0.25	2.51 ± 0.75
58445	35776057	S	1.99 ± 0.42	0.68 ± 0.34
58446	35776058	S	1.27 ± 0.43	1.70 ± 0.98
58520	21432	C	1.66 ± 0.03	1.71 ± 0.03
58521	22082	C	1.65 ± 0.03	1.87 ± 0.04
58663	35776059	S	1.69 ± 0.28	0.79 ± 0.27

Notes: The facility is represented by C-*Chandra*, S-*Swift*, X-*XMM-Newton*, N-*NuSTAR* and Su-*Suzaku*.

Table A2: **UVOT data of Mrk 1018.** Columns include the date of observations and the absorption and host corrected flux.

Date (MJD)	U [mJy]	Date (MJD)	UVW1 [mJy]	Date (MJD)	UVM2 [mJy]	Date (MJD)	UVW2 [mJy]
53587	3.77 ± 0.10	53587	3.56 ± 0.11	53587	3.51 ± 0.06	53587	3.53 ± 0.08
54628	2.86 ± 0.08	54271	2.99 ± 0.09	54628	2.46 ± 0.04	54273	2.92 ± 0.06
56352	0.35 ± 0.04	54275	3.12 ± 0.09	56352	0.34 ± 0.02	54628	2.35 ± 0.05
56450	0.47 ± 0.03	54628	2.60 ± 0.08	56450	0.41 ± 0.02	56352	0.24 ± 0.01
56817	0.08 ± 0.02	56352	0.32 ± 0.02	56817	0.09 ± 0.01	56450	0.39 ± 0.01
57429	0.12 ± 0.02	56450	0.48 ± 0.02	57429	0.07 ± 0.01	56817	0.09 ± 0.01
57434	0.05 ± 0.02	56817	0.13 ± 0.01	57434	0.06 ± 0.00	57429	0.06 ± 0.00
58124	0.07 ± 0.01	57429	0.09 ± 0.01	58362	0.07 ± 0.01	57434	0.06 ± 0.01
58316	0.07 ± 0.01	57434	0.08 ± 0.01	58363	0.06 ± 0.01	58173	0.08 ± 0.00
58362	0.12 ± 0.03	58362	0.12 ± 0.02	58364	0.07 ± 0.01	58362	0.08 ± 0.01
58363	0.05 ± 0.02	58363	0.09 ± 0.01	58365	0.08 ± 0.01	58363	0.08 ± 0.01
58364	0.09 ± 0.03	58364	0.10 ± 0.01	58368	0.06 ± 0.01	58364	0.07 ± 0.01
58365	0.03 ± 0.02	58365	0.10 ± 0.01	58369	0.05 ± 0.01	58365	0.08 ± 0.01
58368	0.07 ± 0.02	58368	0.08 ± 0.01	58370	0.06 ± 0.01	58368	0.07 ± 0.01
58369	0.06 ± 0.02	58369	0.09 ± 0.01	58374	0.06 ± 0.01	58369	0.05 ± 0.01
58370	0.05 ± 0.03	58370	0.13 ± 0.02	58375	0.05 ± 0.01	58370	0.08 ± 0.01
58374	0.09 ± 0.03	58374	0.10 ± 0.01	58375	0.06 ± 0.01	58374	0.07 ± 0.01
58375	0.08 ± 0.03	58375	0.07 ± 0.02	58378	0.07 ± 0.01	58375	0.07 ± 0.01
58375	0.10 ± 0.03	58375	0.09 ± 0.01	58384	0.07 ± 0.01	58375	0.09 ± 0.01
58378	0.04 ± 0.02	58378	0.09 ± 0.01	58385	0.09 ± 0.01	58378	0.07 ± 0.01
58384	0.07 ± 0.03	58384	0.09 ± 0.01	58390	0.06 ± 0.01	58384	0.07 ± 0.01
58385	0.04 ± 0.03	58385	0.09 ± 0.02	58390	0.07 ± 0.01	58385	0.07 ± 0.01
58390	0.08 ± 0.02	58390	0.14 ± 0.02	58391	0.07 ± 0.01	58390	0.08 ± 0.01
58390	0.07 ± 0.02	58390	0.12 ± 0.02	58392	0.06 ± 0.01	58390	0.07 ± 0.01
58391	0.08 ± 0.03	58391	0.14 ± 0.02	58393	0.09 ± 0.01	58391	0.08 ± 0.01
58392	0.07 ± 0.02	58392	0.13 ± 0.02	58395	0.06 ± 0.01	58392	0.08 ± 0.01
58393	0.12 ± 0.03	58393	0.14 ± 0.02	58396	0.06 ± 0.01	58393	0.07 ± 0.01
58395	0.12 ± 0.03	58395	0.10 ± 0.01	58397	0.06 ± 0.01	58395	0.08 ± 0.01
58396	0.05 ± 0.03	58396	0.11 ± 0.02	58399	0.07 ± 0.01	58396	0.06 ± 0.01
58397	0.10 ± 0.03	58397	0.11 ± 0.01	58399	0.10 ± 0.01	58397	0.06 ± 0.01
58399	0.09 ± 0.03	58399	0.12 ± 0.02	58402	0.08 ± 0.01	58399	0.09 ± 0.01
58399	0.07 ± 0.02	58399	0.10 ± 0.01	58406	0.06 ± 0.01	58399	0.08 ± 0.01
58402	0.04 ± 0.02	58402	0.11 ± 0.01	58409	0.09 ± 0.01	58402	0.07 ± 0.01
58406	0.03 ± 0.02	58406	0.11 ± 0.02	58410	0.07 ± 0.01	58406	0.08 ± 0.01
58409	0.00 ± 0.02	58409	0.09 ± 0.01	58412	0.05 ± 0.01	58409	0.07 ± 0.01
58410	0.07 ± 0.02	58410	0.10 ± 0.01	58413	0.05 ± 0.01	58410	0.08 ± 0.01
58412	0.07 ± 0.02	58412	0.09 ± 0.01	58417	0.05 ± 0.01	58412	0.06 ± 0.01
58413	0.06 ± 0.02	58413	0.10 ± 0.01	58418	0.06 ± 0.01	58413	0.07 ± 0.01
58417	0.09 ± 0.03	58417	0.07 ± 0.01	58420	0.07 ± 0.01	58417	0.06 ± 0.01
58418	0.06 ± 0.02	58418	0.09 ± 0.01	58420	0.06 ± 0.01	58418	0.07 ± 0.01
58420	0.01 ± 0.02	58420	0.08 ± 0.01	58422	0.07 ± 0.01	58420	0.06 ± 0.01
58420	0.07 ± 0.02	58420	0.07 ± 0.01	58423	0.06 ± 0.01	58420	0.06 ± 0.01
58422	0.02 ± 0.02	58422	0.07 ± 0.01	58424	0.07 ± 0.01	58422	0.06 ± 0.01
58423	0.10 ± 0.03	58423	0.07 ± 0.01	58425	0.07 ± 0.01	58423	0.07 ± 0.01
58424	0.06 ± 0.02	58424	0.08 ± 0.01	58426	0.05 ± 0.01	58424	0.06 ± 0.01
58425	0.03 ± 0.02	58425	0.09 ± 0.01	58427	0.06 ± 0.01	58425	0.08 ± 0.01
58426	0.05 ± 0.02	58426	0.07 ± 0.01	58428	0.06 ± 0.01	58426	0.06 ± 0.01
58427	0.06 ± 0.02	58427	0.12 ± 0.01	58429	0.05 ± 0.01	58427	0.07 ± 0.01
58428	0.06 ± 0.02	58428	0.09 ± 0.01	58433	0.08 ± 0.01	58428	0.06 ± 0.01
58429	0.05 ± 0.02	58429	0.10 ± 0.01	58434	0.08 ± 0.01	58429	0.07 ± 0.01
58433	0.06 ± 0.03	58433	0.10 ± 0.02	58436	0.07 ± 0.01	58433	0.07 ± 0.01
58434	0.03 ± 0.02	58434	0.09 ± 0.01	58437	0.07 ± 0.01	58434	0.08 ± 0.01
58436	0.06 ± 0.02	58436	0.08 ± 0.01	58439	0.06 ± 0.01	58436	0.07 ± 0.01
58437	0.06 ± 0.03	58437	0.10 ± 0.01	58441	0.06 ± 0.01	58437	0.06 ± 0.01
58439	0.09 ± 0.02	58439	0.11 ± 0.01	58444	0.04 ± 0.01	58439	0.07 ± 0.01
58441	0.04 ± 0.03	58441	0.09 ± 0.02	58445	0.06 ± 0.01	58441	0.08 ± 0.01
58444	0.04 ± 0.02	58444	0.10 ± 0.01	58446	0.05 ± 0.01	58444	0.07 ± 0.01
58445	0.08 ± 0.03	58445	0.08 ± 0.01	58663	0.03 ± 0.01	58445	0.06 ± 0.01
58446	0.10 ± 0.03	58446	0.07 ± 0.01			58446	0.04 ± 0.01
58663	0.05 ± 0.02	58663	0.07 ± 0.01			58663	0.04 ± 0.01

Table A3. VLA data of Mrk 1018. Columns include the date of observation, project name, band, frequency, integrated flux, radio spectral index (α_R) and references.

Date (MJD)	project	band	Frequency [GHz]	F_{int} [mJy]	α_R	References
46032	AU0020	L	1.49	4.21 ± 0.23	0.52 ± 0.07	
		C	4.86	2.29 ± 0.14		
47261	AB0476	C	4.86	1.91 ± 0.23		
47692	AB0540A	C	4.86	2.62 ± 0.16		
47732	AB0540B	C	4.86	2.31 ± 0.17		
49341	AC0308	L	1.4	4.20 ± 0.54		Condon et al. (2002)
50031	AB0628	L	1.4	4.20 ± 0.45		Condon et al. (1998)
50970	AB0878	X	8.46	2.47 ± 0.17	0.30 ± 0.08	
52490	AB0950	L	1.4	4.15 ± 0.25		Becker et al. (2003)
54873	AR685	L	1.4	3.69 ± 0.19		Hodge et al. (2011)
54926	AB1314	L	1.4	3.36 ± 0.20		Becker et al. (2012)
56542	13B-272	L	1.4	3.85 ± 0.31		Heywood et al. (2016)
57481	16A-444	C	5.0	2.56 ± 0.13	0.25 ± 0.10	
		X	10.0	2.16 ± 0.11		
57719	16B-084	X	10.0	1.78 ± 0.09		
57731	16B-084	X	10.0	1.97 ± 0.10		
57768	16B-084	C	5.0	2.07 ± 0.10	0	
58087	VLASS1.1	L	3.0	2.30 ± 0.36		

Table A4. Radio and X-ray luminosity correlation diagram. Columns include the date of radio observation, rescaled radio flux at 5 GHz ($F_{5\text{GHz}}$), the date of X-ray observation, X-ray flux in 2-10 keV band, the observation interval between two bands, the radio luminosity rescaled to 5 GHz ($L_R = \nu L_{5\text{GHz}}$) and X-ray luminosity in 2-10 keV band (L_X).

T_{Radio} (MJD)	$F_{5\text{GHz}}$ [mJy]	$T_{\text{X-ray}}$ (MJD)	$F_{2-10\text{keV}}$ [10^{-12} erg $\text{cm}^{-2}\text{s}^{-1}$]	δT (Day)	$\log(L_R)$ [erg s^{-1}]	$\log(L_X)$ [erg s^{-1}]
54926	2.29 ± 0.24	55015	10.00 ± 0.50	-89	38.63	43.57
56542	2.63 ± 0.31	56450	7.94 ± 0.91	91	38.69	43.47
57481	2.56 ± 0.01	57443	1.27 ± 0.03	38	38.68	42.67
57768	2.07 ± 0.01	57801	2.44 ± 0.02	-33	38.58	42.96
58087	1.97 ± 0.12	58123	2.10 ± 0.10	-36	38.56	42.89